Research Article Vol. 12, No. 7 / July 2025 / Optica 907

OPTICA

Quantitative polarimetric wavefront imaging

BAPTISTE BLOCHET,[1,†,*] GRÉGOIRE LELU,[1,†] MIGUEL A. ALONSO,[2,3] AND MARC GUILLON[1,4,5,6]

[1]Université Paris Cité, CNRS, Saints-Pères Paris Institute for the Neurosciences, F-75006 Paris, France
[2]Aix Marseille Univ, CNRS, Centrale Med, Institut Fresnel, UMR 7249, 13397 Marseille, France
[3]The Institute of Optics, University of Rochester, Rochester, New York 14627, USA
[4]Institut Langevin, ESPCI Paris, Université PSL, CNRS, Paris 75005, France
[5]Institut Universitaire de France, Paris, France
[6]marc.guillon@u-paris.fr
[†]These authors contributed equally to this work.
*baptiste.blochet@u-paris.fr

Received 26 September 2024; revised 17 February 2025; accepted 3 March 2025; published 23 June 2025

Imaging both the polarization and the wavefront of a light beam is a complex task that typically demands several intensity acquisitions. Furthermore, sequential acquisition solutions are incompatible with the monitoring of ultra-fast processes. As a possible solution for single-shot wavefront and full-Stokes polarimetric imaging, we propose here a vector-beam lateral shearing interferometer. The device, composed of a patterned polarization-modulating Hartmann mask placed in close vicinity to a camera, encodes all the information in the fringe pattern of a single-image acquisition. By extending lateral shearing interferometry to vector beams, this work opens avenues for characterizing complex metasurfaces and biological samples.

https://doi.org/10.1364/OPTICA.542225

1. INTRODUCTION

While optical sensors can only measure the intensity, an important part of the information is typically encoded in the spatial phase (or wavefront) of the beam, as well as in its polarization state (the relative amplitude and phase between two orthogonal polarization components). Imaging the wavefront and/or polarization is of key importance in many applications: phase imaging is typically required for cophasing segmented laser arrays [1] or imaging thin transparent objects [2,3] where it can provide a quantitative measure of the dry mass of cells [4]; polarimetric imaging is of interest for quantitative biological and biomedical applications [5,6], but also for non-destructive testing [7] as well as machine vision under specular reflections [8] and through fog [9] for hidden target detection [10]; and simultaneous phase and polarimetric imaging is of high importance for vectorial adaptive optics [11], metrology of metasurfaces [7], optical tomography [12], and single-molecule localization microscopy [13]. Phase and polarimetric imaging typically demand three and four intensity acquisitions at least, respectively. In total, 12 images are thus recorded for a complete determination of the electromagnetic field in the optical range. Unfortunately, no simple instrument exists that can fully image electromagnetic wavefields in the optical frequency range in a single acquisition step.

Many techniques have been developed to image either polarization or phase, but far fewer solutions have been proposed to image both [14–16]. The mere combination of the independently developed phase and polarization imaging modalities faces major obstacles associated with cumulative technical complexity and cost of the resulting optical systems [17] and are additionally either sequential, incomplete in polarization [14], or have low resolution [15,16].

Here, we propose an original method to image both the wavefront and the full polarization state of a light beam in a single acquisition step. The technique we propose is based on the same principles as lateral shearing interferometry (LSI) [18,19], a simple reference-free achromatic and quantitative wavefront imaging technique. In LSI, a phase grating is used as a Hartmann mask placed at a close distance from a camera sensor, generating a dense grid of foci. LSI is thus the high-resolution analog of the highly popular Shack–Hartmann wavefront sensors. In LSI, the intensity is encoded in the low spatial frequency content of the camera pattern, while wavefront gradients are encoded as spatial frequency modulations. Similarly, we suggest here using a polarization-modulating Hartmann mask to encode the full-Stokes image as well as the wavefront of the beam. Our polarimetric approach can be categorized as a division of the channeled-imaging technique [17,20,21], in contrast with the division of aperture [20], division of amplitude [22,23], and division of focal plane [24,25] solutions. The solution we propose for full-Stokes polarimetric wavefront imaging is compatible with partially coherent polarization states, can work over a spectral range larger than 200 nm, provides high-resolution images (up to 410×410 px^2 for a 2048×2048 px^2 camera), and is potentially compatible with a compact and monolithic design.

This paper presents the sequential development and validation process of the instrument, beginning with the concept of polarimetric lateral shearing interferometry, implemented here using a patterned linearly birefringent mask. Next, we describe the numerical optimization of the mask, followed by its experimental characterization. Key aspects of the experimental implementation are then outlined, including the phase and polarization reconstruction algorithm and the experimental setup. Finally, we demonstrate the resolution and accuracy of the instrument, showcasing its capabilities for typical metrological applications over a tunable spectral range.

2. DESIGN AND CHARACTERIZATION OF THE POLARIMETRIC LSI

A. Principle of Polarimetric Wavefront Sensing

A structured polarization-modulating Hartmann mask placed (or imaged) at a close distance d from a camera sensor [Fig. 1(a)] yields intensity patterns sensitive both to the polarization state and to the beam wavefront. This can be shown by generalizing the wavefront sensing (WFS) equation [18,26] to the case of vector beams in the paraxial approximation, based on the Jones matrix of the mask (Supplement 1, Section S2). The intensity at the camera sensor mask is given by

$$\boldsymbol{I}(\boldsymbol{r}) = \boldsymbol{C}\left[\boldsymbol{r} + d\frac{\boldsymbol{k}_\perp(\boldsymbol{r})}{k_0}\right]\boldsymbol{s}(\boldsymbol{r}), \tag{1}$$

where $\boldsymbol{r} = (x, y)$ is the transverse position vector, k_0 is the wavenumber of the light beam, and $\boldsymbol{C} = (\boldsymbol{c_0}, \boldsymbol{c_1}, \boldsymbol{c_2}, \boldsymbol{c_3})$ is a four-column matrix containing the four respective normalized Stokes calibration intensity patterns: $\boldsymbol{c_j}$ is the calibration intensity pattern representing the corresponding component of the Stokes vector s_j only, in the case of a planar wavefront illumination. It is worth noting that Eq. (1) was obtained assuming a spatially coherent light beam characterized by a Stokes vector $\boldsymbol{s} = (s_0, s_1, s_2, s_3)$ and a local transverse wavevector $\boldsymbol{k}_\perp = k_x\boldsymbol{e_x} + k_y\boldsymbol{e_y}$.

The local Stokes vector and the local transverse wavevector of an unknown spatially coherent beam can then be recovered by solving Eq. (1) if the calibration patterns $\boldsymbol{C}$ are known.

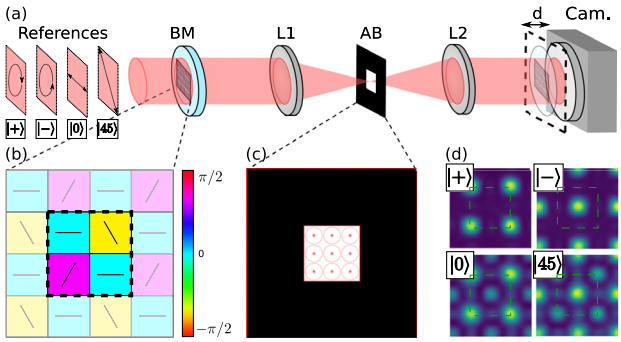

Fig. 1. Principle of the optical system. (a) A periodic birefringent mask (BM) is imaged at a distance d from a camera sensor with a telescope. This polarization-modulating diffractive mask whose unit cell is shown in (b) generates nine main diffraction orders (c); the remaining orders could be optionally filtered out by using an aperture block (AB). (d) Specific intensity grids, forming a basis, are then obtained at the camera plane for impinging beams having polarization states defining a non-zero volume inside the Poincaré sphere.

B. Case of a Linearly Birefringent Mask

In this work, we consider a polarization-modulating Hartmann mask exhibiting linear birefringence. A linearly birefringent plate with slow and fast optical path differences (OPDs), δ_s and δ_f, changes an impinging circular polarization state $\boldsymbol{\sigma}_\pm$ to

$$\boldsymbol{E}_{\text{out},\pm} = e^{i\phi}\left[\cos\left(\frac{\varphi}{2}\right)\boldsymbol{\sigma}_\pm + ie^{\pm 2i\theta}\sin\left(\frac{\varphi}{2}\right)\boldsymbol{\sigma}_\mp\right], \tag{2}$$

where $\phi = k(\delta_s + \delta_f)/2$ is the mean phase delay, $\varphi = k(\delta_s - \delta_f)$ is the retardance with k being the wavenumber, and θ is the polar angle of the slow-axis orientation (Supplement 1, Section S1). By patterning the orientation θ of the slow axis of the mask, the factor $e^{\pm 2i\theta}$ thus allows imprinting a phase grating modulation as required by LSI. In addition, partial conversion of the $\boldsymbol{\sigma}_\pm$ components of the impinging beam to the cross-polarized states, driven by the retardance φ, yields interferences accounting both for their respective amplitudes and relative phases. As a result, when placed at a close distance d from a camera sensor, this mask yields a shear between the diffracted orders, resulting in interference patterns sensitive to the wavefront of the beam, while the partial polarization conversion creates interferences between orthogonal components of the impinging beam.

Note that the phase imprinted onto the converted cross-polarized circular beam is solely determined by the geometric patterning of the birefringence axis angle θ, so that the phase grating is perfectly achromatic. This principle is at the basis of numerous applications harnessing the Pancharatnam–Berry geometric phase in optics [27,28]. Nevertheless, although the phase modulation is perfectly achromatic, the polarization-conversion efficiency varies with the wavelength. This limitation is equivalent to that of usual LSI implementations, wherein the diffraction efficiency, driven by the phase modulation depth of the mask, also depends on the wavelength. In both cases, the short propagation distance to the camera results in wavelength-independent fringe periods.

C. Optimization of a Birefringent Grating for Polarimetric LSI

The birefringent grating needs to be optimized to minimize the reconstruction noise in the polarimetric and wavefront measurements. This numerical optimization process is specifically performed under the assumption of small intensity pattern distortions, considering small propagation distances d and wavefront gradients. Under this approximation, s_j and $\boldsymbol{k}_\perp(\boldsymbol{r})$ can be computed by linearizing Eq. (1). The wavefront map is then derived from $\boldsymbol{k}_\perp(\boldsymbol{r})$ through numerical two-dimensional integration [29,30]. For sufficiently small angles and distances d, the magnitude of the dimensionless displacement amount $\boldsymbol{\kappa} = \frac{d}{\Lambda k_0}\boldsymbol{k}_\perp$ is much smaller than the unity, where Λ is the period of the intensity grid.

A first-order Taylor expansion of $\boldsymbol{C}$ in Eq. (1) yields

$$\boldsymbol{I} \approx \boldsymbol{C}\boldsymbol{s} + \kappa_x\partial_x\boldsymbol{C}\boldsymbol{s} + \kappa_y\partial_y\boldsymbol{C}\boldsymbol{s}, \tag{3}$$

where $\partial_j\boldsymbol{C}$ is the derivative of $\boldsymbol{C}$ along $j \in \{x, y\}$, multiplied by the length scale Λ. Over one macro-pixel m defined by one grid period, Eq. (3) can be written as a matrix system, assuming that the beam state is essentially uniform over the macro-pixel extent:

$$\boldsymbol{I_m} \approx \boldsymbol{A_m}\hat{\boldsymbol{s}}, \tag{4}$$

where $\boldsymbol{A_m} = (\boldsymbol{C}, \partial_x \boldsymbol{C}, \partial_y \boldsymbol{C})$ is the 12-column transfer function matrix, and $\hat{\boldsymbol{s}} = (\boldsymbol{s}^T, \boldsymbol{s_x}^T, \boldsymbol{s_y}^T)^T$ is the vector describing the corresponding beam state. For a spatially coherent beam, Eq. (4) must be solved subject to $\boldsymbol{s_x} = \kappa_x \boldsymbol{s}$ and $\boldsymbol{s_y} = \kappa_y \boldsymbol{s}$, thus imposing that $\boldsymbol{s}$, $\boldsymbol{s_x}$, and $\boldsymbol{s_y}$ are collinear. In order to allow the simultaneous determination of the vectors $\boldsymbol{s}$ and $\boldsymbol{\kappa}$, Eq. (4) must always be invertible, for all $\boldsymbol{s} \neq \boldsymbol{0}$. We thus optimized the birefringent Hartmann mask for any possible beam state. To achieve so in the most general case, we considered minimizing the Cramér–Rao lower bound of the 12-dimensional system [Eq. (4)], based on the calculation of the Fisher information matrix [31]. Assuming a normal noise distribution with uniform variance over all camera pixels, the Fisher information matrix is proportional to $\boldsymbol{F} \propto \boldsymbol{A_m}^T \boldsymbol{A_m}$ (Supplement 1, Section S3). As a metric for optimizing the birefringent mask, we chose to minimize the highest Cramér–Rao lower bound, corresponding to the least well-conditioned eigenstate. This is obtained by minimizing the condition number of $\boldsymbol{A_m}$, namely the ratio λ_1/λ_{12}, where λ_1 and λ_{12} are the largest and smallest eigenvalues of $\boldsymbol{A_m}$, respectively. In practice, we designed the mask as a birefringent square grating with a unit cell composed of 2×2 domains of uniform slow-axis orientations [see Fig. 1(b)]. Due to technological limitations in the fabrication process of the liquid-crystal (LC) mask, the retardance is uniform all over the mask. A genetic algorithm was then used to jointly optimize the six parameters of the grating: the (uniform) retardance value, the four slow-axis angles in the unit cell, and the propagation distance d between the mask and the camera plane.

D. Optimized Birefringent Grating

The numerical optimization process converged toward the pattern shown in Fig. 1(b), exhibiting slow-axis angles θ with spacings of $\pi/3$ and a retardance $\varphi = 1.16\pi/2$ rad. Several optimal distances d from the camera are possible: $d \in \{0.22, 0.28, 0.72, 0.78\}\Lambda_T$, where d is expressed in units of Talbot length $\Lambda_T = 2\Lambda^2/\lambda$. The field generated by this mask exhibits nine Fourier components arranged in a 3×3 square, as illustrated in Fig. 1(c). The optimization algorithm was run by filtering only these nine lowest orders in order to ensure high-resolution imaging capabilities. Since the polarimetric and wavefront information is fully carried by the 3×3 main diffracting orders generated by the mask, the power spectrum of the intensity at the camera—given by the autocorrelation of this pattern—contains 5×5 spatial frequencies. Therefore, the minimal size of a macro-pixel is 5×5 camera pixels for the pattern to be resolved (and the matrix $\boldsymbol{A_m}$ to be invertible). In this configuration, the aperture block (AB) shown in Figs. 1(a) and 1(c) is not necessary.

The cross-polarized diffracted orders yield nine sheared replicas of the beam at a short distance d, interfering all together as well as with the unconverted and undiffracted contribution of the cross-polarized impinging contribution (the diagonal term of the Jones matrix). The theoretical expression of the Jones matrix of a linearly birefringent mask, placed at a distance d and expressed in the circular polarization basis, is given by

$$J = \begin{pmatrix} \cos(\varphi/2) & -Q^{(+)} \sin(\varphi/2) \\ Q^{(-)} \sin(\varphi/2) & \cos(\varphi/2) \end{pmatrix}, \tag{5}$$

where the spatially patterned factor $Q^{(\pm)}$ for our optimized mask is given by

$$Q^{(\pm)} = \tilde{q}_2 \pm i\tilde{q}_1, \tag{6}$$

with

$$\tilde{q}_1 = \frac{1}{4} - \frac{3}{8}\tilde{\nu}^2[\cos(x+y) - \cos(x-y)], \tag{7a}$$

$$\tilde{q}_2 = -\frac{\sqrt{3}}{4}\tilde{\nu}(\sin x - \sin y), \tag{7b}$$

and $\tilde{\nu} = 4/\pi \exp(-i2\pi d/\Lambda_T)$ (Supplement 1, Section S4).

E. Experimental Characterization of the Mask

A mask was manufactured (Thorlabs Inc., USA) according to the optimized design parameters given above and shown in Fig. 1(b). In Fig. 1(d), four typical (experimental) calibration intensity patterns obtained at 532 nm and at a distance $d = 0.22\Lambda_T$ from this mask are shown over two grating periods. Interestingly, for circular polarization incidence, the obtained birefringent Hartmann mask exhibits an array of focal points that closely resembles those utilized in conventional Shack–Hartmann wavefront sensing schemes. For the sake of illustration, an optional square-shaped aperture block [AB in Figs. 1(a) and 1(c)] was deliberately introduced to select and exhibit the role of the nine main orders at play. As discussed before, this spatial filter is not necessary because higher spatial frequencies are naturally filtered by camera sampling at the Shannon–Nyquist criterion limit.

The reciprocal condition number $C_{12} = \lambda_{12}/\lambda_1$ of the transfer function matrix $\boldsymbol{A_m}$ of our mask, which indicates how well the beam information can be retrieved, is shown in Fig. 2: C_{12} is plotted as a function of the wavelength over a 200 nm spectral range and the distance d. This first experimental characterization was carried out using a fiber-coupled supercontinuum laser (ElectroVis-470, LEUKOS, France) combined with a computer-controlled filter box (Bebop, LEUKOS, France) that provides bandwidths down to 5 nm. The line profile at the design wavelength ($\lambda = 532$ nm) is shown in Fig. 2(b), demonstrating good agreement with the numerical expectation up to a favorable experimental extra offset of 2.5% that we attribute to fabrication imperfections. It must also be pointed out that these results demonstrate that the mask can effectively operate over a broad spectral range, due to the achromatic nature of the phase imprinted onto the converted cross-polarized circular beam, which is solely determined by the geometric patterning of the birefringence axis angle. The capability of our polarimetric WFS approach to work in broadband conditions was also numerically evaluated. The results indicate that the reciprocal condition number C_{12} only experiences

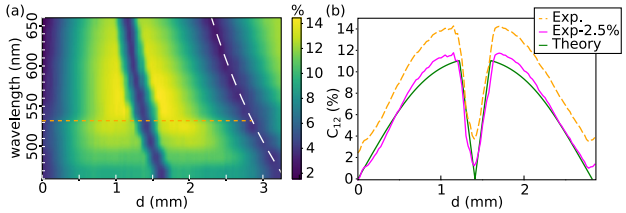

Fig. 2. Reciprocal condition number $\boldsymbol{C_{12}}$ of the transfer matrix. Experimental values are shown in (a) as a function of the wavelength and the distance between the mask image and the camera d, demonstrating workability over a 200 nm large spectral range (460 − 660 nm). The white-dashed line represents half the Talbot length Λ_T, with the pattern being symmetrically repeated at greater distances d. A line profile along the orange-dashed line is shown in (b) for $\lambda = 532$ nm ($\Lambda_T = 5.72$ mm) and is compared with the theoretical curve. The experimental curve exhibits a ≃2.5% extra offset.

a slight decrease, of the order of 10%, under broadband illumination ($\Delta\lambda = 200$ nm), confirming that the system remains well conditioned (Supplement 1, Fig. S1).

3. EXPERIMENTAL IMPLEMENTATION

A. Image Reconstruction Algorithm

Image reconstruction is achieved by solving Eq. (1) in $\boldsymbol{s}$ and $\boldsymbol{k}_\perp$. In practice, we solve Eq. (1) with an iterative algorithm, which allows both (i) managing distortions beyond the range of validity of the first-order Taylor expansion [Eq. (3); see Supplement 1, Fig. S4], and (ii) integrating the spatial coherence prior about the beam (one single $\boldsymbol{k}_\perp$ for any $\boldsymbol{s}$ component). The justification and full description of the algorithm can be found in Supplement 1, Section S5 and Fig. S5. In a nutshell, the algorithm consists of iteratively (i) estimating $\boldsymbol{s}$ from $\boldsymbol{C}\boldsymbol{s} = \boldsymbol{I_m}$, (ii) synthesizing the corresponding calibration pattern $\boldsymbol{c_e} = \sum_{j=0}^{3} s_j \boldsymbol{c_j}$, (iii) estimating $\boldsymbol{\kappa}$ by solving $\boldsymbol{A_e}\boldsymbol{\kappa} = \boldsymbol{I_m} - \boldsymbol{c_e}$ with $\boldsymbol{A_e}$ (of rank two) defined as $\boldsymbol{A_e} = (\partial_x \boldsymbol{c_e}, \partial_y \boldsymbol{c_e})$, and (iv) performing a non-rigid registration of $\boldsymbol{C} = (\boldsymbol{c_0}, \boldsymbol{c_1}, \boldsymbol{c_2}, \boldsymbol{c_3})$ according to $\boldsymbol{\kappa}$ (see Supplement 1, Fig. S5). The equations used to estimate $\boldsymbol{s}$ and $\boldsymbol{\kappa}$ [steps (i) and (iii)] must be solved for each period of the diffraction grating, representing a single sampling point. Numerically, we considered a sliding Gaussian window (waist $w = 2/3\Lambda$), using the Lucas–Kanade method [32]. In this method, the sought-for state $\hat{\boldsymbol{s}}$ (polarization state and wavefront gradients) is assumed to be uniform over the considered window width. We found that the algorithm typically converges after a few steps (see Supplement 1, Fig. S6 and Fig. S7). Compared to a one-step first-order reconstruction algorithm, the iterative approach improved the image resolution and enabled quantitative wavefront measurements.

B. Experimental Setup

The full description of the experimental setup is given in Supplement 1, Fig. S3. The samples shown in Figs. 3 and 4 are illuminated with collimated light beams generated from a white LED after passing through a 532/10 nm excitation filter. The sample in Fig. 5 is illuminated using four different spectral bands, selected with bandpass filters at 532/10, 580/10, 690/10, and 540/40 nm. The polarization state of the illumination beam is controlled by a custom-built computer-controlled polarization state generator, which has been calibrated for all illumination spectra used. The samples are imaged into the mask with a magnification of 1:1, and the mask is then imaged at a distance d from the camera sensor with a magnification of 1:2 to achieve proper sampling of the mask by the camera sensor. For the experiments shown in Figs. 3 and 4, the birefringent grating has a period of $\Lambda = 78$ μm, corresponding to six camera pixels after magnification. In contrast, for Fig. 5, the grating period is $\Lambda = 65$ μm, which corresponds to the theoretical minimum of five pixels after magnification. The distance d between the image of the mask and the camera was tuned at $d = 0.18\Lambda_T = 1.03$ mm, $d = 0.32\Lambda_T = 1.83$ mm, and $d = 0.32\Lambda_T = 1.27$ mm (at 532 nm), respectively, for Figs. 3–5.

4. RESULTS

A. Validation Using a Birefringent USAF Target

To demonstrate the performance of the quantitative phase and polarimetric imager, a linear birefringent USAF target (R3L1S1B, Thorlabs Inc., USA) was imaged [Fig. 3(a)]. This sample was chosen because it is based on a geometric phase modulation that is linked to the modulation of the polarization state. Therefore, it allows for a cross-validation of the accuracy of the polarization and wavefront measurements. Namely, according to Eq. (2), the orientation of the LC molecules $\theta(x, y)$ can be recovered either from the polarization image reconstruction only [Figs. 3(a) and 3(b)] or from the wavefront image of the converted cross-polarized circular component [Fig. 3(c)]. Phase and polarization images are obtained using the iterative algorithm described above (see Supplement 1, Section S5 and Fig. S5). To further validate these results, the orientation of the LC molecules was also estimated by rotating the sample between two cross-polarizers [green strip in Fig. 3(d)].

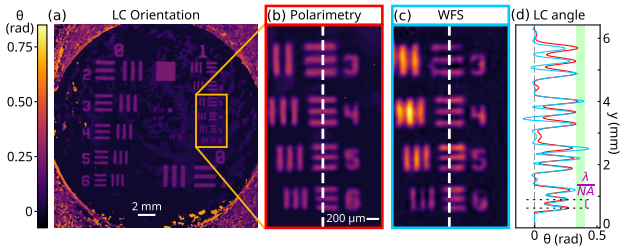

Fig. 3. Quantitative phase and polarimetric measurements of a birefringent USAF target. (a) Full-field image of the orientation θ of the LC of the target obtained through polarimetric measurements. (b) Zoom of a region reaching the resolution limit of the instrument. (c) The orientation θ over the very same region is obtained from the wavefront of the cross-polarized circular contribution of the beam. (d) Line profiles of θ along the white-dashed lines in (b) and (c). The green strip in (d) indicates the additional experimental measurement of θ in motifs estimated by rotating the sample between two cross-polarizers. The smallest resolved lines are very close to the expected resolution limit λ/NA.

First, the LC orientation θ was estimated from the reconstructed polarization images. To improve the measurement accuracy, several acquisitions were performed with our device with varying input polarization states to measure the Mueller matrix of the sample. The LC orientation θ was then determined by fitting the measured Mueller matrix to a model of linear retarders using a Levenberg–Marquardt non-linear least square algorithm [33]. The LC orientation image reconstructed using this method is presented in Figs. 3(a) and 3(b).

Second, the wavefront was recovered from a single image acquisition obtained by illuminating the sample with a $\boldsymbol{\sigma}_-$ polarized beam. The $\boldsymbol{\sigma}_+$ converted beam therefore carries a spatial phase $e^{-2i\theta}$ [Eq. (2)]. The retardance of the sample, specified by the manufacturer as $\varphi = 280 \pm 20$ nm, was experimentally measured at $\varphi = 320 \pm 14$ nm. At $\lambda = 532$ nm, this retardance value leads to a large conversion of the incident circular polarization state into the cross-polarized state, with only a fraction of 10% of power remaining in the $\boldsymbol{\sigma}_-$ channel (see Supplement 1, Fig. S8a). The obtained LC orientation image is shown in Fig. 3(c) after background subtraction (see Supplement 1, Fig. S8b). Notably, the near half-wave retardance of the sample used is suboptimal for measuring the geometrical phase. A more balanced power distribution between σ_+ and σ_- contributions would enhance the discrimination between the mean phase ϕ and the geometrical phase term θ [Eq. (2)].

Third, an additional experimental validation was performed by rotating cross-polarizers, revealing that the LC on the patterns is rotated by $21 \pm 2°$ relatively to the background ones [green strip in Fig. 3(d)].

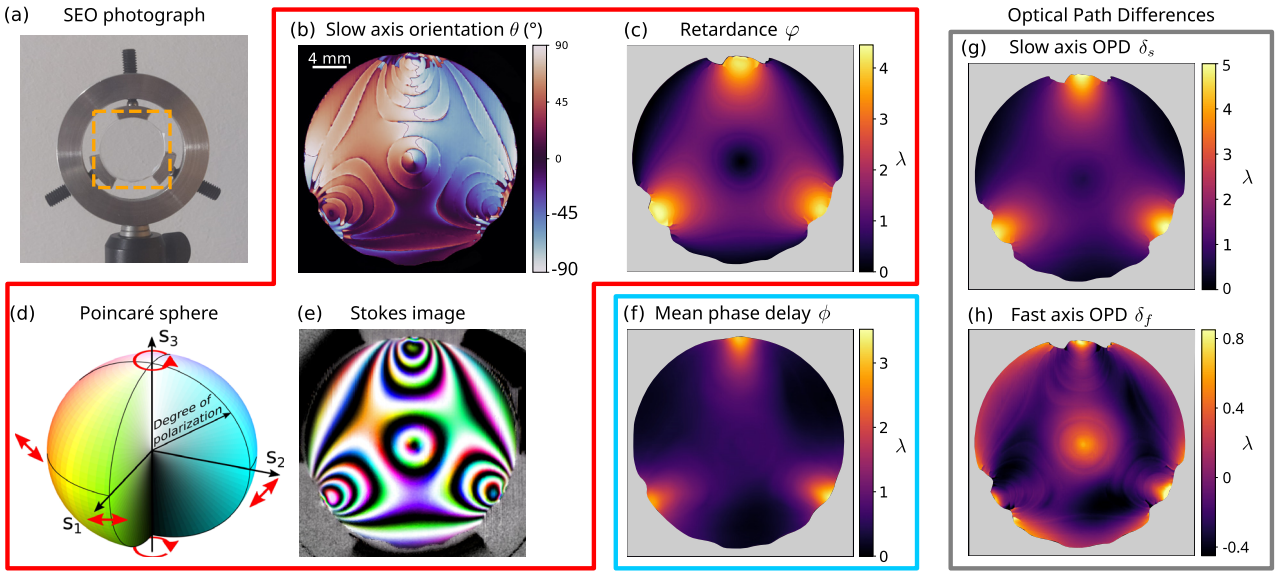

Fig. 4. Single-shot polarimetric (red box) and wavefront (blue box) imaging of an SEO. (a) Regular photograph of the custom-made SEO. (b) Slow-axis orientation θ exhibiting the topological singularity and (c) retardance φ, both obtained from the polarimetric measurement. (d), (e) The full-Stokes image of the SEO obtained from an incoming $\boldsymbol{\sigma}_-$ polarization state (e) together with its color coding of the polarization state represented on the Poincaré sphere (d). (f) The mean phase delay ϕ recovered by integration of the displacement map $\boldsymbol{\kappa}$. (g), (h) Optical path differences of the slow (g) and fast (h) axes of the SEO obtained from the retardance φ and the mean phase delay ϕ.

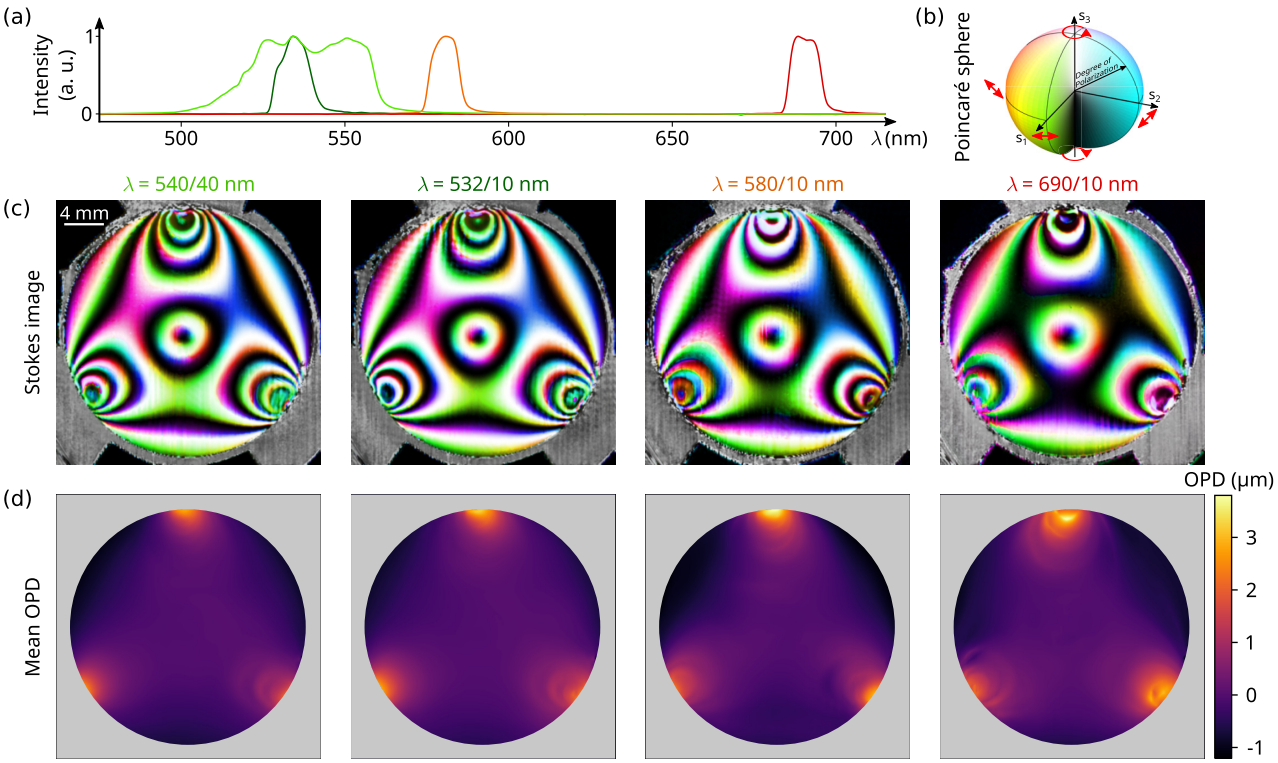

Fig. 5. Single-shot polarimetric wavefront imaging of an SEO for different illumination wavelengths and spectra. (a) Illumination spectra. (b), (c) Poincaré sphere and Stokes mapping. (d) Mean optical path delays (OPDs).

As a result, polarimetric measurement [Fig. 3(b)], wavefront measurements [Fig. 3(c)], and our third validating experiment exhibit good agreement with each other, as can be seen on the line profiles in Fig. 3(d). The closest resolved lines in the sample are spaced by $\simeq$290 μm, very close to the estimated resolution limit of our imaging system: $\lambda/\mathrm{NA} \simeq 270$ μm.

B. Metrology of a Stressed Engineered Optic

A custom-built stress-engineered optics (SEO) [34,35] was considered as a sample [Fig. 4(a)]. SEOs have been used for producing structured polarization beams [36,37], for polarization measurements of sparse objects [38–40], and as Fourier filters for dipole spread function engineering [41], in particular for

superlocalization microscopy [42]. The SEO used here consists of a circular window of N-BK7 glass stressed at three points arranged in an equilateral triangle. This stress induces an anisotropic linear birefringence pattern exhibiting a $-1/2$-charged line dislocation at the center. Thus, a $\boldsymbol{\sigma}_{\pm}$ polarized beam yields a transmitted $\boldsymbol{\sigma}_{\mp}$ carrying orbital angular momentum. We imaged the SEO under $\boldsymbol{\sigma}_{-}$ polarized light beam illumination with the aim of characterizing both the birefringence pattern and geometric aberrations (that are not visible by polarimetric imaging). Phase and polarization images are obtained using the same iterative algorithm as presented before.

In a single acquisition step, we retrieve full-Stokes information as well as wavefront distortions. Next, relying on Eq. (2), the physical parameters of the SEO can be extracted: the slow-axis orientation θ [Fig. 4(b)], the retardance φ [Fig. 4(c)], and the average phase delay ϕ [Fig. 4(f)]. The Stokes image is shown in Fig. 4(e) with a hue–saturation–lightness color code [Fig. 4(d)].

By considering an impinging $\boldsymbol{\sigma}_{-}$ circular polarization state on the SEO, from Eq. (2), we obtain

$$\tan^2\left(\frac{\varphi}{2}\right) = \frac{s_0 + s_3}{s_0 - s_3}, \tag{8}$$

$$ie^{-2i\theta}\sin\varphi = s_1 + is_2, \tag{9}$$

so that φ and θ can thus be computed up to a sign ambiguity accounting for the uncertain identification of the fast and slow axes when imaging at a single wavelength. For this reason, their respective images in Figs. 4(b) and 4(c) have been unwrapped: the sign was changed for every zero crossing of $\sin\varphi$, starting from the center where φ is known to be zero for symmetry reasons (see Supplement 1, Fig. S9 for the raw results and the unwrapping process). The slight discontinuity lines in Fig. 4(b) are due to this unwrapping process. The slow-axis orientation accounts for the refractive index increase along the constraint lines. Finally, the integration of the displacement map $\boldsymbol{\kappa}$ allows recovering the average optical path difference map ϕ imprinted to the beam [Fig. 4(f)]. From ϕ and φ, the slow and fast OPDs, δ_s and δ_f, respectively, can be plotted [Figs. 4(g) and 4(h)]. The ability to measure not only the retardance of the sample but also the average OPD demonstrates the practical interest of coupling polarimetric and wavefront imaging modalities to access full optical characterization.

C. Spectral Resilience

For imaging applications, using a low-coherence light source is preferable as it minimizes interference artifacts that typically degrade imaging capabilities. The experimental images shown in the previous sections demonstrate that our system is compatible with illumination beams having 10 nm wide spectral bandwidth, which corresponds to a correlation length of the order of 30 μm. This is in contrast with a system that places a mask in a Fourier plane that typically requires smaller spectral widths [43].

In our case, experimental data support that our system remains well conditioned over the $460-660$ nm spectral range under quasi-monochromatic illumination (Fig. 2) as well as for broad spectrum beams (Supplement 1, Fig. S1 and Fig. S2 demonstrate this for up to 200 nm). Moreover, the mask can be placed over a considerably large range of distances d. Thus, we now experimentally validate that quantitative phase and polarimetric measurements can be obtained at different wavelengths and spectral widths for a given mask placed at a given fixed distance $d = 0.32\Lambda_T$. We measured the phase and polarimetric images of the SEO sample using four different incident spectra: 532/10, 580/10, 690/10, and 540/40 nm [Fig. 5(a)]. The reconstructed full-Stokes images and the mean OPD images of the SEO under these four illumination conditions are shown in Figs. 5(c) and 5(d), respectively. The variations in polarization state observed in the Stokes images [Fig. 5(c)] for different central wavelengths λ are mostly due to the drift of the retardance with the wavenumber [$\varphi = 2\pi(\delta_s - \delta_f)/\lambda$]. The dispersion of the N-BK7 glass can indeed be reasonably neglected here so that the slow δ_s and fast δ_f optical path differences can be considered achromatic. Under this same assumption, the measured mean optical path difference $(\delta_s + \delta_f)/2$ is also expected to be almost achromatic, in agreement with the experimental images [Fig. 5(d)]. Near the three stress points of the SEO, some reconstruction artifacts are observed because of large phase and retardance gradients.

5. DISCUSSION

We demonstrated the possibility of extending the principle of multiwave lateral shearing interferometry to vector beams and to encode the full-Stokes polarization state of a beam in addition to its wavefront. Since more information is multiplexed at the camera plane, more interfering waves are required, and one sampling point requires more camera pixels (5×5 at least), thus providing 400×400 full-Stokes polarimetric and wavefront images from a single 4 Mpx camera.

Interestingly, the dimension of the optimized transfer function matrix $\boldsymbol{A_m}$ in Eq. (4) is 12. If the constraint about the collinearity of $\boldsymbol{s}$, $\boldsymbol{s_x}$, and $\boldsymbol{s_y}$ is relaxed, our polarimetric WFS instrument turns out to be sensitive to the polarization-resolved spatial coherence of the light source [44]. Indeed, considering a density of incoherent classical emitters $\rho(\boldsymbol{s}, \boldsymbol{\kappa})$, the intensity at the camera sensor is $\boldsymbol{I} = \boldsymbol{C}\,\overline{\boldsymbol{s}} + \partial_x \boldsymbol{C}\,\overline{\kappa_x \boldsymbol{s}} + \partial_y \boldsymbol{C}\,\overline{\kappa_y \boldsymbol{s}}$, where the bar notation denotes averaging over the emitters' distribution: $\overline{\kappa_j \boldsymbol{s}} = \iint \kappa_j \rho(\boldsymbol{s}, \boldsymbol{\kappa}) \mathrm{d}^4\boldsymbol{s}\,\mathrm{d}^2\boldsymbol{\kappa}$.

Finally, the mask optimized in this paper is designed based on specific statistical assumptions regarding noise and wavefront distortion magnitudes, but other masks can be designed similarly for different cases following the same principles.

Funding. Agence Nationale de la Recherche (ANR-21-CE24-0014-01, ANR-20-CE42-0006, ANR-24-CE42-1853).

Acknowledgment. The authors acknowledge Sophie Brasselet and Pascal Berto for stimulating discussions, Anis Aggoun for his support with the Python codes, and Dorian Bouchet for his remarks about the paper. This work was partly funded by the French Research National Agency and the French government's Future Investment Program (Stratex Université Paris Cité). Mark Guillon acknowledges the support from the Institut Universitaire de France, and Miguel A. Alonso acknowledges the support from ANR.

Disclosures. The authors declare no conflicts of interest.

Data availability. Data underlying the results presented in this paper are not publicly available at this time but may be obtained from the authors upon reasonable request.

Supplemental document. See Supplement 1 for supporting content.

REFERENCES

1. M. Deprez, C. Bellanger, L. Lombard, *et al.*, "Piston and tilt interferometry for segmented wavefront sensing," Opt. Lett. **41**, 1078–1081 (2016).

2. Y. Park, C. Depeursinge, and G. Popescu, "Quantitative phase imaging in biomedicine," Nat. Photonics **12**, 578–589 (2018).
3. P. C. Chaumet, P. Bon, G. Maire, *et al.*, "Quantitative phase microscopies: accuracy comparison," arXiv, (2024).
4. R. Barer, "Interference microscopy and mass determination," Nature **169**, 366–367 (1952).
5. L.-H. Yeh, I. E. Ivanov, T. Chandler, *et al.*, "Permittivity tensor imaging: modular label-free imaging of 3D dry mass and 3D orientation at high resolution," Nat. Methods **21**, 1257–1274 (2024).
6. C. He, H. He, J. Chang, *et al.*, "Polarisation optics for biomedical and clinical applications: a review," Light Sci. Appl. **10**, 194 (2021).
7. Q. Song, A. Baroni, P. C. Wu, *et al.*, "Broadband decoupling of intensity and polarization with vectorial Fourier metasurfaces," Nat. Commun. **12**, 3631 (2021).
8. X. Huang, C. Wu, X. Xu, *et al.*, "Polarization structured light 3D depth image sensor for scenes with reflective surfaces," Nat. Commun. **14**, 6855 (2023).
9. J. Fade, S. Panigrahi, A. Carré, *et al.*, "Long-range polarimetric imaging through fog," Appl. Opt. **53**, 3854–3865 (2014).
10. F. Goudail and J. S. Tyo, "When is polarimetric imaging preferable to intensity imaging for target detection?" J. Opt. Soc. Am. A **28**, 46–53 (2011).
11. C. He, J. Antonello, and M. J. Booth, "Vectorial adaptive optics," eLight **3**, 23 (2023).
12. S. Song, J. Kim, T. Moon, *et al.*, "Polarization-sensitive intensity diffraction tomography," Light Sci. Appl. **12**, 124 (2023).
13. P. Bon, J. Linarès-Loyez, M. Feyeux, *et al.*, "Self-interference 3D super-resolution microscopy for deep tissue investigations," Nat. Methods **15**, 449–454 (2018).
14. S. Aknoun, P. Bon, J. Savatier, *et al.*, "Quantitative retardance imaging of biological samples using quadriwave lateral shearing interferometry," Opt. Express **23**, 16383–16406 (2015).
15. Z. Yang, Z. Wang, Y. Wang, *et al.*, "Generalized Hartmann-Shack array of dielectric metalens sub-arrays for polarimetric beam profiling," Nat. Commun. **9**, 4607 (2018).
16. T. Wakayama, A. Zama, Y. Higuchi, *et al.*, "Simultaneous detection of polarization states and wavefront by an angular variant micro-retarder-lens array," Opt. Express **32**, 2405–2417 (2024).
17. H. Luo, K. Oka, E. DeHoog, *et al.*, "Compact and miniature snapshot imaging polarimeter," Appl. Opt. **47**, 4413–4417 (2008).
18. J. Primot, "Three-wave lateral shearing interferometer," Appl. Opt. **32**, 6242–6249 (1993).
19. J. Primot and L. Sogno, "Achromatic three-wave (or more) lateral shearing interferometer," J. Opt. Soc. Am. A **12**, 2679–2685 (1995).
20. J. S. Tyo, D. L. Goldstein, D. B. Chenault, *et al.*, "Review of passive imaging polarimetry for remote sensing applications," Appl. Opt. **45**, 5453–5469 (2006).
21. M. W. Kudenov, M. J. Escuti, E. L. Dereniak, *et al.*, "White-light channeled imaging polarimeter using broadband polarization gratings," Appl. Opt. **50**, 2283–2293 (2011).
22. E. Arbabi, S. M. Kamali, A. Arbabi, *et al.*, "Full-Stokes imaging polarimetry using dielectric metasurfaces," ACS Photonics **5**, 3132–3140 (2018).
23. N. A. Rubin, G. D'Aversa, P. Chevalier, *et al.*, "Matrix Fourier optics enables a compact full-Stokes polarization camera," Science **365**, eaax1839 (2019).
24. D. Gottlieb and O. Arteaga, "Mueller matrix imaging with a polarization camera: application to microscopy," Opt. Express **29**, 34723–34734 (2021).
25. J. Zuo, J. Bai, S. Choi, *et al.*, "Chip-integrated metasurface full-Stokes polarimetric imaging sensor," Light Sci. Appl. **12**, 218 (2023).
26. M. R. Teague, "Image formation in terms of the transport equation," J. Opt. Soc. Am. A **2**, 2019–2026 (1985).
27. S. Pancharatnam, "Generalized theory of interference and its applications," Proc. Indian Acad. Sci. **44**, 247–262 (1956).
28. M. V. Berry, "Quantal phase factors accompanying adiabatic changes," Proc. Roy. Soc. London A **392**, 45–57 (1984).
29. L. Huang, M. Idir, C. Zuo, *et al.*, "Comparison of two-dimensional integration methods for shape reconstruction from gradient data," Opt. Lasers Eng. **64**, 1–11 (2015).
30. T. Wu, P. Berto, and M. Guillon, "Reference-less complex wavefields characterization with a high-resolution wavefront sensor," Appl. Phys. Lett. **118**, 251102 (2021).
31. S. M. Kay, *Fundamentals of Statistical Processing, Volume I: Estimation Theory* (Prentice Hall, 1993).
32. B. Lucas and T. Kanade, "An iterative image registration technique with an application to stereo vision (IJCAI)," in *7th International Joint Conference on Artificial Intelligence* (1981).
33. K. Levenberg, "A method for the solution of certain non-linear problems in least squares," Q. Appl. Math. **2**, 164–168 (1944).
34. A. K. Spilman and T. G. Brown, "Stress birefringent, space-variant wave plates for vortex illumination," Appl. Opt. **46**, 61–66 (2007).
35. A. K. Spilman and T. G. Brown, "Stress-induced focal splitting," Opt. Express **15**, 8411–8421 (2007).
36. A. M. Beckley, T. G. Brown, and M. A. Alonso, "Full Poincaré beams," Opt. Express **18**, 10777–10785 (2010).
37. A. M. Beckley, T. G. Brown, and M. A. Alonso, "Full Poincaré beams II: partial polarization," Opt. Express **20**, 9357–9362 (2012).
38. R. D. Ramkhalawon, T. G. Brown, and M. A. Alonso, "Imaging the polarization of a light field," Opt. Express **21**, 4106–4115 (2013).
39. B. G. Zimmerman and T. G. Brown, "Star test image-sampling polarimeter," Opt. Express **24**, 23154–23161 (2016).
40. S. Sivankutty, E. R. Andresen, G. Bouwmans, *et al.*, "Single-shot polarimetry imaging of multicore fiber," Opt. Lett. **41**, 2105–2108 (2016).
41. A. Vella and M. A. Alonso, "Optimal birefringence distributions for imaging polarimetry," Opt. Express **27**, 36799–36814 (2019).
42. V. Curcio, L. A. Alemán-Castañeda, T. G. Brown, *et al.*, "Birefringent Fourier filtering for single molecule coordinate and height super-resolution imaging with dithering and orientation," Nat. Commun. **11**, 5307 (2020).
43. N. A. Rubin, P. Chevalier, M. Juhl, *et al.*, "Imaging polarimetry through metasurface polarization gratings," Opt. Express **30**, 9389–9412 (2022).
44. B. Stoklasa, L. Motka, J. Rehacek, *et al.*, "Wavefront sensing reveals optical coherence," Nat. Commun. **5**, 3275 (2014).